Flame Speed and Particle Image Velocimetry Measurements of Laminar Burning Velocities and Markstein Numbers of some Hydrocarbons.

D. Bradley*, M. Lawes, M. E. Morsy

School of Mechanical Engineering, University of Leeds, Leeds LS2 9JT, UK.

*Corresponding author: D.Bradley@leeds.ac.uk

Abstract

Particle Image Velocimetry, PIV, is described for measuring laminar burning velocities during flame propagation in spherical explosions, by the measurement of the flame speed and gas velocity just ahead of the flame. Measurements made in this way are compared with those obtained from the flame speed method, which is based on the flame front propagation speed and the ratio of unburned to burned gas densities. Different values arise between the two methods, and the principal reason is the common assumption in the flame speed method that the burned gas density is at the equilibrium, burned gas, adiabatic temperature. When allowance is made for the effects of flame stretch rate and Lewis number on this density, the differences in burning velocities are significantly decreased. The PIV methodology enables mass rate of burning velocities to be expressed in terms of the burning velocity at zero stretch rate and the Markstein numbers for strain rate and flame curvature. Burning velocities and Markstein numbers are presented for methane, i-octane, ethanol, and n-butanol over a range of equivalence ratios at atmospheric pressure and, in the case of n-butanol, also over a range of pressures. Account is taken of the low stretch rate at which a laminar flame becomes unstable, and, below which, the burn rate increases due to the enhanced flame surface area. The critical stretch rates for the transition are identified. In measuring Markstein numbers, there is a dependency upon the isotherm employed for the measurement of the stretch rate. This aspect is studied by comparing measurements with two different isotherms. It is concluded that the measured PIV flame measurements might under-estimate the Markstein numbers by about 12%.

Keywords: Laminar burning velocity; Flame instability; Markstein numbers; spherical explosion flames.

Nomenclature

A	m^2	flame surface area
c_p	$\mathrm{J/kg.K}$	specific heat
D	m^2/s	thermal diffusivity $(\lambda/\rho C_p)$
D_{im}	m^2/s	minority species diffusion coefficient
K		Karlovitz stretch factor $(\delta\,\alpha_{sr}/u_l + \delta\,\alpha_{cr}/u_l)$
K_{cl}		critical Karlovitz number
K_c, K_s		Karlovitz curvature and strain rate factors, $(\delta\alpha_{cr}/u_l)$, $(\delta\alpha_{sr}/u_l)$
L_b	m	flame speed Markstein length
L_{cr},L_{sr}	m	curvature and strain Markstein lengths, respectively, associated with u_{nr}
L_u	m	Markstein length for u_n
Le		Lewis number $(\lambda/\rho D_{im} c_p)$
Ma		Markstein number
Ma_b		flame speed Markstein number
Ma_{cr},Ma_{sr}		curvature and strain Markstein numbers, respectively, associated with u_{nr}
P	Pa	initial pressure
Pe_{cl}		critical Peclet number, r_{cl}/δ
Pr		Prandtl number $(c_p\eta/\lambda)$
r_{cl}	m	critical flame radius
r_u	m	cold flame front radius
S		flame speed factor, Eq. (4)
S_n	m/s	stretched laminar flame speed
S_s	m/s	unstretched laminar flame speed
t	s	time
T_b	K	adiabatic equilibrium burned gas temperature
$\bar{T}_b$	K	burned gas mean temperature
T_u	K	unburned gas temperature
u_g	m/s	outwards gas velocity
u_l	m/s	PIV, unstretched laminar burning velocity, u_n at $\alpha = 0$
u_{la}	m/s	adiabatic density, unstretched laminar burning velocity, see Eq. (5)
u_{lr}	m/s	PIV u_l with no radiative loss
u_{ls}	m/s	density corrected, unstretched laminar burning velocity, $\rho_b = \bar{\rho}_b$ in Eq.(5) and $u_{ls} = u_{la}$
u_n	m/s	flame entrainment laminar velocity
u_{nr}	m/s	stretched laminar mass burning velocity expressing mass burning rate , see Eqs. (7) and (8).

Greek Symbols

α	1/s	flame stretch rate
α_{cl}	1/s	critical stretch rate for flame instability
α_{cr}	1/s	curvature strain rate
α_{sr}	1/s	strain rate
γ		ratio of specific heats

δ	m	flame thickness $(\nu/u_l)/Pr$	φ		equivalence ratio
λ	$\mathrm{J/m.K.s}$	thermal conductivity	ρ_b	$\mathrm{kg/m^3}$	adiabatic-burned gas density
μ	$\mathrm{kg/m.s}$	dynamic viscosity	$\bar{\rho}_b$	$\mathrm{kg/m^3}$	mean burned gas density
ν	$\mathrm{m^2/s}$	kinematic viscosity	ρ_u	$\mathrm{kg/m^3}$	unburned gas density

1. Introduction

An early critical review of laminar burning velocity, u_l, described six different measurement techniques, including particle tracking, for measuring velocities, yet it omitted any treatment of flame stretch rate [1]. At an early stage, it became apparent that more complete data on flow velocities, from particle tracking [2] and hot wire anemometry [3], yielded values of u_l that differed from those obtained from more traditional techniques. Later, Direct Numerical Simulations [4] showed that burning velocities based solely upon schlieren measurements of flame speeds in strongly radiating spherical explosion flames would be under-predicted, and would be more accurately measured with particle image velocimetry, PIV.

Yufei Dong et al. [5] employed PIV in the flow configuration ahead of a stagnation plate, whilst Balusamy et al. [6] employed it to measure the laminar burning velocities of propane/air mixtures in spherical explosion flames. Varea et al. [7] also used such flames to measure laminar burning velocities and Markstein lengths of methane, ethanol and i-octane/air. Measurements of laminar burning velocity by this technique are not widespread because of the inherent experimental difficulties and necessary post-processing of a large number of data points. As a result, the spherical flame explosion technique, based solely on flame speed measurements, has become widely employed for this purpose. This flame speed method necessitates assumptions about the adiabatic density of the burned gas that are not required with PIV, which simultaneously measures the flame speed and gas velocity just ahead of the flame. The difference in these values gives a burning velocity that can yield a mass rate of burning. In addition, both the flame curvature and strain rate contributions to the flame stretch rate, α, can readily be found.

The present paper reports PIV measurements in spherical explosions, from which burning velocities can also be derived from the flame speed measurements. The velocity measurements also enable entrainment and mass rate of burning velocities to be found, along with flame stretch rates and associated Markstein numbers. In the flame speed method of measuring burning velocity, it is often assumed that the burned gas density at zero stretch rate is that of an adiabatic flame under equilibrium conditions, ρ_b. This tends to be an under-estimation, giving burning velocities that are shown to be about 4-11 % low. A modification of this approach is developed, involving the burned gas density of the stretched flame, entirely in the regime of stable propagation, prior to the development of unstable flames at low stretch rate. In the stable regime, the mean burned gas density, $\bar{\rho}_b$, is larger than ρ_b, and depends on the stretch rate, α, and Lewis number, Le. There is little change in $\bar{\rho}_b$ before the instability develops. Values of $\bar{\rho}_b$ yield values of burning velocities that are closer to those determined by PIV. The PIV method provides more complete information on flame propagation and, consequently, more accurate data on burning velocities, the influences of flame stretch rates, the onset of flame instabilities, and radiative energy exchanges. Burning velocities are presented from both of the flame speed methods, as well as the PIV-derived values for methane, n-butanol, i-octane and ethanol mixtures with air and, in the case of n-butanol, over a range of pressures.

The paper develops a methodology for correcting burning velocities, measured by the flame speed method, due to it not having an adiabatic value for the burned gas density. Normal strain rate laws and Markstein numbers are only applicable during the propagation of stable flames and a methodology for defining this regime is explained. Errors arise in the determination of Markstein numbers, if the temperature of the associated isotherm is too low, and this effect is quantified.

2. PIV velocities, flame speeds, stretch rates and Markstein numbers

The basic PIV velocities are related by:

$$u_n = S_n - u_g \, . \tag{1}$$

Here u_n is the stretched laminar entrainment velocity, S_n, the stretched flame speed, and u_g the maximum outwards gas velocity component, normal to the flame. The overall stretch rate, α, of a spherical explosion flame, of leading edge radius, r_u, is given by:

$$\alpha = \frac{1}{A}\frac{dA}{dt} = \frac{2}{r_u}\frac{dr_u}{dt} = \frac{2}{r_u}S_n, \tag{2}$$

with $S_n = dr_u/dt$.

The flame entrainment velocity, u_n, is related to the flame speed, S_n, by [8]:

$$u_n = \bar{\rho}_b S_n/\rho_u + r_u/(3\rho_u)\,(d\bar{\rho}_b/dt), \tag{3}$$

with $\bar{\rho}_b$, the mean density within the radius, r_u.

A stable flame takes time to develop from the initiating spark plasma. Whilst the flame is developing with a small radius, r_u, $\bar{\rho}_b$, is higher than the density of the adiabatically burned equilibrium gas, ρ_b, at a temperature, T_b. Measurements of u_n were only made, at constant pressure, after a stable flame had become established. With continuing flame growth, the final term in Eq. (3) decreases and finally becomes negligible. During this time, this changing condition is expressed by a flame speed factor:

$$S = u_n\rho_u/S_n\rho_b. \tag{4}$$

S starts with a value of about 2 and diminishes towards unity as $\bar{\rho}_b$, in Eq. (3), decreases and approaches ρ_b [8]. With the flame stretch rate approaching zero, the flame speed approaches a stretch-free value of S_s, with the burning velocity, u_{la}. Neglecting radiative heat transfer from the burned gas, its density at the adiabatic equilibrium temperature of, T_b, in Eq. (4) yields:

$S = 1$ and a laminar burning velocity, $u_{la} = (\rho_b/\rho_u)S_s$. (5)

This expression is widely used in the flame speed method for measuring u_{la}. The flame speed, S_n, at a stretch rate α, is related to S_s by a flame speed Markstein length, L_b, in the relationship [9]:

$$S_s - S_n = L_b\alpha. \tag{6}$$

The mass burning rate velocity, u_{nr}, at constant pressure for the formation of completely burned gas [10, 11] is related to u_n and S_n by [8]:

$$u_{nr} = (S_n - u_n)\left(\frac{\rho_u}{\rho_b} - 1\right)^{-1} = u_g\left(\frac{\rho_u}{\rho_b} - 1\right)^{-1}, \tag{7}$$

There are two contributions to α, one due to strain rate, α_{sr} , $2u_g/r_u$, the other to flame curvature, α_{cr}, $2u_n/r_u$, with $\alpha = \alpha_{sr} + \alpha_{cr}$. Each has an associated Markstein length, L_{sr} and L_{cr}, and the influence of flame stretch rate upon the burning velocity is expressed by [8]:

$$u_l - u_{nr} = L_{sr}(2u_g/r_u) + L_{cr}(2u_n/r_u), \tag{8}$$

with u_l the stretch-free laminar burning velocity with $\alpha = 0$. Markstein numbers are obtained by normalising these lengths with the laminar flame thickness, given by $(\nu/u_l)/Pr$, where ν is the mixture kinematic viscosity, and Pr the Prandtl number, both obtained at the unburned gas temperature using the Gaseq code [12]. Also for the derivation of accurate Markstein lengths, the isotherm upon which α is based in Eq. (2) should be closer to the burned gas, than to the unburned gas temperature [13].

3. Apparatus

Measurements of S_n and u_g were made in spherical explosion flames at 0.1 MPa for methane, i-octane and ethanol/air mixtures at 300 K, 358 K and 360 K, respectively, over a range of equivalence ratios, and also for n-butanol/air mixtures at 383 K between 0.1 and 0.5 MPa. The explosions occurred in a spherical stainless steel explosion vessel of 190 mm inner radius. Flame images were obtained through three pairs of orthogonal windows of 150 mm diameter, enabling flame radii to be measured up to 60 mm, after a stable flame had been established at a radius of about 10 mm. An electric heater aided evaporation. Mixture temperatures were measured with a sheathed chromel–alumel thermocouple and mixing was facilitated by four fans, driven by electric motors, located close to the vessel wall [14].

A double pulsed Nd:YAG laser (DM60-DH, Photonics), generated pulses of 12 mJ at a wavelength of 532 nm at 5 KHz. These, created a sheet about 0.5 mm thick to illuminate the uniformly dispersed seeding particles in the flow. The laser beam was expanded into a vertical sheet in the middle of the explosion vessel, as indicated in Fig. 1. The measuring system was comprised of two spherical lenses of -650 mm and 300 mm focal lengths and cylindrical lens of -20 mm focal length. A high-speed camera, perpendicular to the laser sheet, recorded a 12-bit image pair of 1024×1024 pixels at a frequency of 5 kHz. The camera was fitted with a macro-Nikon lens of 108 mm focal length, coupled with an optical band pass filter centered at 532 nm to minimise the effect of flame luminosity. Six jet atomisers (9010F0021, DANTEC) generated olive oil droplets $< 1\ \mu m$, with a boiling temperature of 570 K. The particle density was 0.51 (particles/pixel). Their evaporation defined the flame location as close to the 570 K isotherm. For comparison, in the widely used flame speed method, the flame is often located by a schlieren front. Based on the structure of a stoichiometric CH_4/air flame, this is approximately the 856 K isotherm [15].

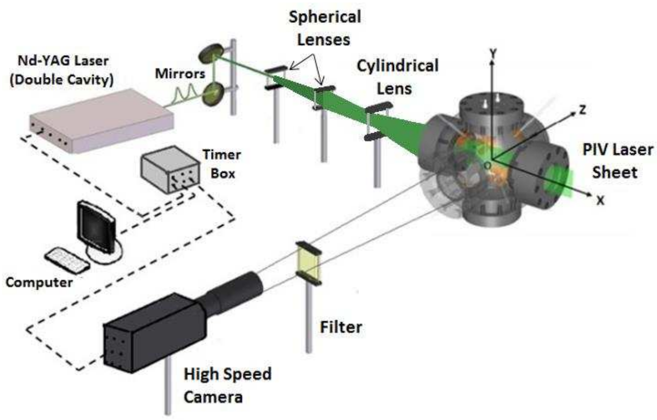

Fig. 1. Optical configuration.

Image analysis and the derivation of flame speed employed computational software developed by the Dantec Dynamics Company. The first stage identified the location of the flame edge, tracking its progression from one image to the next, using a phase boundary detection tool. The flame edge was first located and its progression tracked, by the evaporative disappearance of the oil particles, enhanced by increasing the contrast. The second step, corrected for unwanted light sheet non-uniformities. The burned gas boundary was located with sub-pixel resolution. The detected flame edges were smoothed by a low pass filter to remove noise from the digitisation steps and a least squares algorithm calculated the best fit circle to the flame edge and the corresponding flame radius. The flame speed, associated with the 570 K isotherm, could then be found from the temporal evolution of the flame front.

Balusamy et al. [6] used an adaptive algorithm to measure directly the local, radially outwards, unburned gas velocity, at entry to the flame front. In the present work, an adaptive algorithm was employed within the Dantec software, in an Adaptive PIV Method. This is an iterative and automatic way of calculating velocity vectors, based on the seeding particle density. It assumes that all seeding particles evaporate completely at the iso-surface. The orientation of individual interrogation areas, IA, were iteratively adjusted to fit the local seeding densities and velocity gradients. The appropriate IA size was automatically determined for each individual IA, by specifying maximum and minimum size limits. A first iteration always used the largest IA size, which was reduced in subsequent iterations. This allowed reduction of IA sizes where the particle density was sufficiently high. The minimum IA determined the location and magnitude of vectors. This location was chosen to be associated with the edge of the minimum IA. This minimum IA employed 8 pixels along the flame front and 2 pixels in the normal direction to the flame (0.86 mm × 0.21 mm), while the maximum was (8 × 8 pixels ~ 0.86 × 0.86 mm). To characterise the velocity profile ahead of the flame front, a sub-pixel tool was developed, linked to the Dantec software to achieve the value of the minimum IA with one pixel step. An example of an instantaneous gas velocity profile for a methane/air flame is presented in Fig. 2, in which zero distance locates the evaporation isotherm.

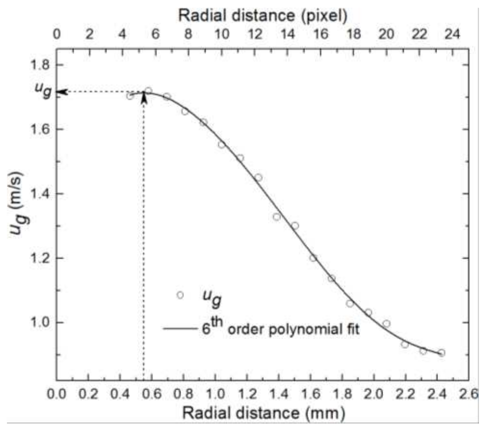

Fig. 2. Gas velocity ahead of flame, CH_4/ air, φ = 1.0, at 0.1 MPa, 300 K.

The maximum gas velocity, u_g, is obtained by fitting the velocity profile to a 6th order polynomial, which gives the highest value of R^2. This maximum value is located about 2–8 pixels ($0.21 - 0.86$ mm) ahead of the evaporation isotherm. Computational studies show a sharp change in gas velocity within the flame zone, with a much smaller variation ahead of the flame [10], as indicated by the profile of measured values, with the maximum value arrowed, in Fig. 2. This adaptive PIV method was used alongside a developed program to calculate the burning velocity. The program calculated the burning velocity from the flame edge profiles and the average value of the maximum unburned gas velocity measurements. More details concerning the data processing are to be found in the supplementary material [S1].

The temperature of 570 K, associated with the disappearance of the evaporating droplets, is probably too low for a front that yields the value of the stretch rate, and a schlieren front close to 860K [15] is preferable. High speed schlieren cine photography therefore was employed to study the effect of the isotherm on measurements of L_b. The technique allows the visual detection of the flame front through the density gradients between the burned and unburned mixtures, caused by the varying degrees of light refraction. A schematic figure of the schlieren optical configuration can be found in the supplementary material [S2]. A near point source of light was provided by a 20 mW (regulated to 5mW), 635 nm LED laser. This expanded on to a f -1000 mm plano-convex lens, collimating a 150 mm beam through the vessel and its contents to another f -1000 mm plano-convex lens. This focused the beam on to a variable diameter iris (1-15 mm). The camera was positioned to give a field of view of 110 mm. This took full advantage of the camera resolution of 1024×1024 pixels with ~ 0.11 mm/pixel. This resolution was more than sufficient to capture a defined flame edge, whilst allowing an ample sampling rate of 5 kHz.

Figure 3 shows two flame images of an ethanol/air mixture, φ = 0.8, at 0.1 MPa and 360 K, recorded by both PIV and schlieren techniques. The same image analysis and derivation of flame speed identified the flame edges, shown be the white circles. A slight deformation of the flame can be observed, but this did not induce any significant departure from sphericity. The near constant maximum gas velocity profile around the flame also indicated that buoyancy effects were negligible.

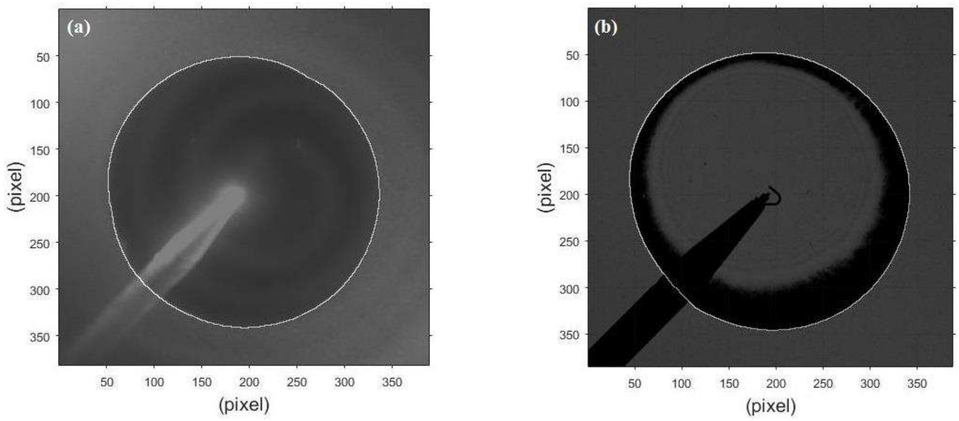

Fig. 3. Flame images of lean ethanol/air mixture, φ=0.8 at 0.1 MPa and 360 K. (a) PIV image, α =140.7 (1/s) and S_n=2.30 m/s. (b) Schlieren image, α =144.2 (1/s) and S_n=2.18 m/s. Scale (0.11 mm/pixel). White circles show flame edges.

4. Experimental methodology

4.1. Stretch rate isotherms

Flame speed, S_n, is plotted against the stretch rate, α, given by Eq. 2, from which the flame speed Markstein length, L_b, is found using Eq. (6). The flame speed is almost independent of the chosen isotherm, but the flame stretch rate also depends on the changing radius of the isotherm, see Eq. (2). An isotherm close to the temperature of the burned gas might be regarded as closest to expressing the rate of formation of burned gas, akin to u_{nr}, Ma_{sr} and Ma_{cr} [8]. Beeckmann et al. [16] showed that PIV and schlieren techniques yield nearly identical Markstein lengths, for a methane/air mixture, φ =1.1 at 0.25 MPa and 298 K. Giannakopoulos et al. [13] showed isotherms in the reaction zone to be more reliable than those in the preheat zone for measuring Markstein numbers.

Measured flame speeds from both the PIV and schlieren images, plotted against α, are compared in Fig. 4, for C_2H_5OH/air flames at different equivalence ratios, φ, at 0.1 MPa, and an initial temperature of 360 K. Those based on PIV Mie scattering images, shown by the full lines, are close to isotherms in the region of 570 K, in contrast to the schlieren images, shown by the broken lines, corresponding to isotherms at about 860 K. As in [13], the higher temperatures gives the higher L_b, between 4-12 % higher than the lower temperatures. For the same two temperatures, but using the theoretical propane/air data in [13] the Markstein numbers would be 50-90% higher at the higher temperature.

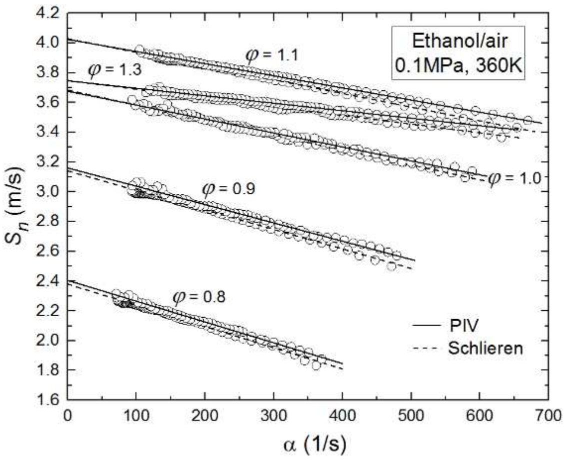

Fig. 4. Variations of PIV and schlieren S_n values with φ for ethanol/air mixtures at 0.1 MPa and 360 K. Full and dashed lines denote linear relationship for L_b through PIV and schlieren points, respectively.

In [13] plateau temperatures are evaluated, at which there is no further change in Markstein number with isotherm temperature. For the conditions in Fig. 4, a suitable plateau isotherm would be that at least 1440 K, (4×T_u). When extrapolated to this temperature, values of L_b at 570 and 860 K give values of L_b between 5 and 18 % higher than those measured at the seed disappearance isotherm, and 3-5% higher than those at the schlieren front. Throughout the present study L_b is measured at the PIV droplet disappearance isotherm, and the underestimation is in the higher of the two ranges.

4.2. Stretch rate effects

The flame speed method of determining u_{la} employs Eq. (6), with S_n plotted against α, given by Eq. (2); S_n is extrapolated to zero stretch rate, where $S_n = S_s$, and $u_{la} = (\rho_b/\rho_u)S_s$. Figure 5 shows such a plot for CH_4/air, φ = 1.0, at 0.1 MPa and 300 K. Values on the y axes are so chosen that the horizontal dashed line in the figure shows S_s on the secondary S_n axis and u_{la} from Eq. (5) on the burning velocity axis, with ρ_b/ρ_u calculated from the Gaseq code [12]. Also plotted are PIV values of u_n from Eq. (1). Because S, and hence u_n/S_n, always decrease in an explosion, as S_n increases, u_n must decrease, as in the figure, and, from Eq. (7), u_{nr} must increase, also as shown.

Values of u_{nr} were found from PIV data using Eq. (7) and L_{sr} and L_{cr} by numerical iteration of the u_{nr} data. In a first iteration, L_{sr} and L_{cr} in Eq. (8) were assumed equal. This yielded an optimal value for this mixture of 0.26 mm, labelled L in Fig. 5. Further iterations with separate values of L_{sr} and L_{cr} yielded the values given on the figure. The second iteration step plotted u_{nr} against α_{sr} and α_{cr} separately. This gave initial values of the corresponding L_{sr} and L_{cr}. The third step inserted these initial values into a program in which a series of iterations computed the associated values of u_{nr} from Eq. (8). These were sensitive to the combination of L_{sr} and L_{cr}. Those that gave the highest value of R^2 were adopted. These were L_{sr}= 0.29 mm and L_{cr} = 0.21 mm for methane/air mixtures, φ = 1.0, at 0.1 MPa and 300 K. This procedure was followed for all mixtures. Plots of $u_{nr} = u_g\left(\frac{\rho_u}{\rho_b} - 1\right)^{-1}$, from Eq. (7) against α when extrapolated to $\alpha = 0$, yielded the PIV value of u_l in Eq. (8), appropriate to u_{nr}.

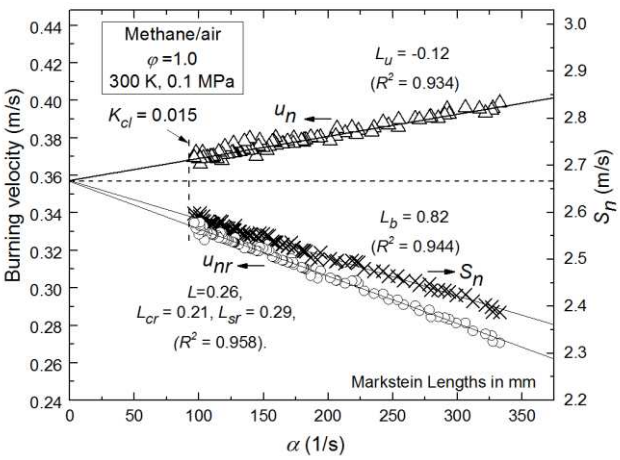

Fig. 5. Variations of S_n, u_n, and u_{nr} with flame stretch rate methane/air mixtures, φ = 1.0, at 0.1 MPa and 300 K. Dashed horizontal line links u_n ($= u_l$) and S_n ($= S_s$) in Eq. (5).

Although a value of L_u in, $u_l - u_n = L_u\alpha$, is given in Fig. 5, Eq. (3) shows u_n, is not a sole variable with α, but depends upon other factors. Only in the later stages does it become a true burning velocity. Because L_u lacks the consistency of a Markstein length, no attempt is made to feature it or evaluate its two components.

In Fig. 5, the validity of the two experimental lines is confined to the markers. At the early, higher, values of α the small radius flame has characteristics of both a spark plasma and developing reactions, before transformation into a flame. Low spark ignition energies were employed and the minimum flame radius was about 10 mm. Between this radius and the upper limit of 60 mm, depending upon the mixture, it was possible for Darius-Landau and thermo-diffusive instabilities to develop at a stretch rate, $\alpha_{cl.}$ The critical radius is r_c, and the critical Peclet number, r_c/δ, is Pe_{cl}. The cellular flame structure so created increases S_n [17, 18]. At this critical condition, the Karlovitz stretch factor, K, = $\alpha\delta_l/u_l$ attains a critical condition, with $\alpha = \alpha_{cl}$, and is given by [19]:

$$K_{cl} = (2\sigma/Pe_{cl})[1 + (2Ma_b/Pe_{cl})]^{-1}. \tag{9}$$

Instabilities develop at values of K less than this value.

The experimental values of S_n and u_n, plotted in Fig. 5, cover the entire stable regime. All values of K_{cl} are taken from the values for different fuel/air mixtures, in [20]. The corresponding stability limit, in terms of α, is indicated by the short vertical line, K_{cl} = 0.015 in Fig. 5. In some instances, just prior to the rapid increase in flame speed, values of S_n became oscillatory. Eq. (8) is the practical formulation of the mass rate of burning, but its validity does not extend into the regime of unstable flames, below α_{cl} down to the value of u_l at $\alpha = 0$, which is imaginary.

4.3. Burned gas density

Only if reaction has been completed adiabatically, is Eq. (5) valid. Clavin and Williams [21] show the value of burned gas density to be dependent upon α and the Lewis number, Le. The deviation of the mean burned gas temperature, $\bar{T}_b$, from the adiabatic burned gas temperature, T_b, is given [11,22] by:

$$\frac{\bar{T}_b - T_b}{T_b} = \frac{D}{(u_{la})^2}\left(\frac{1}{Le} - 1\right)\alpha\,. \tag{10}$$

Here, D, is the thermal diffusivity of the mixture, obtained, like T_b, from [12], for the initial conditions of T_u and P. Measurements of temperature distributions have confirmed the general validity of this equation [11,22]. It shows that high α and Le values can, under some circumstances, create mean temperatures significantly below adiabatic values. As α decreases the temperature slowly recovers, but only with Le = 1.0 can $\bar{T}_b = T_b$. The changes in α are known, as the flame radius increases during the period of flame stability. Figures 6 and 7, derived from this equation, show $\bar{T}_b$ and $\bar{\rho}_b$ plotted against flame radius, r_u. For the stoichiometric CH_4 mixture of Fig. 6

with Le = 0.99 [23, 24] and D = $2.01 \times 10^{-5}\ m^2/s$ [12], the figure shows the near unity value of Le ensures early attainment of the adiabatic equilibrium values, T_b and ρ_b, in accordance with Eq. (5). This explains the good convergence of the S_n and u_n straight lines at α = 0 in Fig. 5, giving $u_l = u_{la}$ = 0.358 ± 0.005 m /s.

In sharp contrast, is the stoichiometric n-C_4H_9OH mixture at 383 K and 0.1 MPa, with Le = 1.58 [25] and $D = 2.72 \times 10^{-5}\ m^2/s$ [12]. Here the high Le ensures $\bar{T}_b$ does not attain T_b in Fig.7, and $\bar{\rho}_b > \rho_b$. Figure 8 shows data for the same mixture, but with $\bar{T}_b$ and $\bar{\rho}_b$ at 0.5 MPa, $Le = 1.12$ and $D = 5.6 \times 10^{-6}\ m^2/s$ [12]. The figure shows the increase in pressure to lead to a rather more rapid attainment of adiabatic equilibrium, attributable to the decreases in both Le and D.

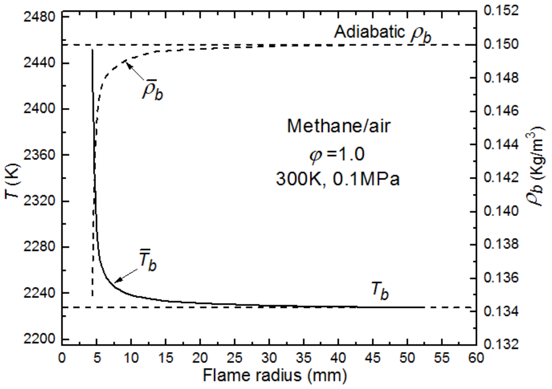

Fig. 6. Computed burned gas temperature and density CH$_4$/air, φ = 1.0, at 300 K and 0.1 MPa, Le = 0.991.

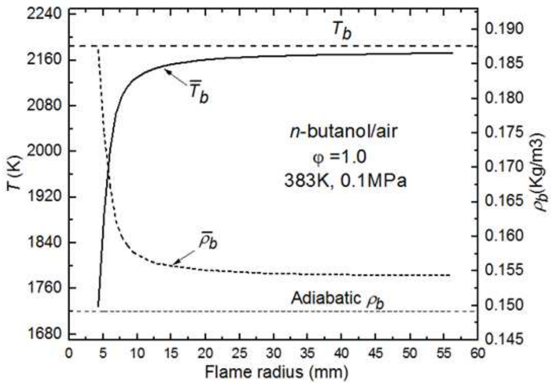

Fig. 7. Computed burned gas temperature and density for n-C_4H_9OH /air, φ = 1.0 at 383 K and 0.1 MPa, Le = 1.58.

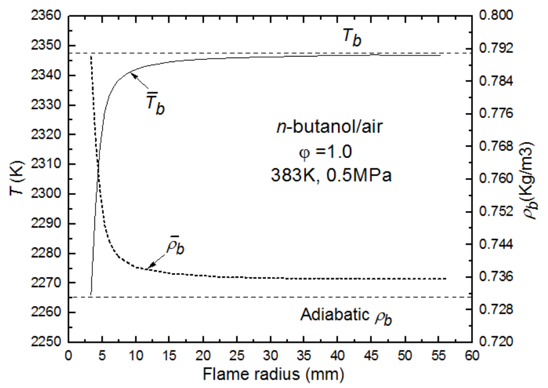

Fig. 8. Computed burned gas temperature and density for n-C_4H_9OH /air, φ = 1.0 at 383 K and 0.5 MPa, Le = 1.12.

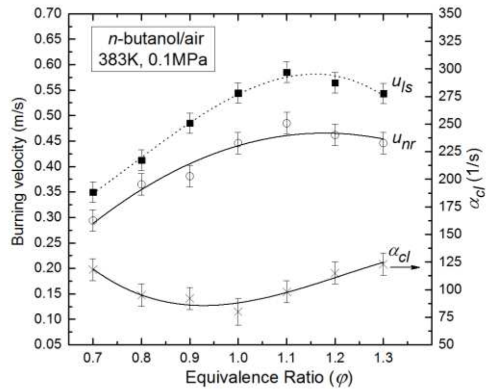

Fig. 9. PIV values of u_{nr} at the boundary values of critical stretch rate, α_{cl}, and values of u_{ls} for n-butanol/air at 0.1 MPa and 383 K.

Mean values, $\bar{\rho}_b$, within the stable extrapolation range of S_n, were found in this manner during explosions. There is little change in $\bar{\rho}_b$ during the developed stable flame propagation. To find the stretch-free value of burning velocity with this modified the flame speed method, S_n is plotted against α down to zero, and the mean value of $\bar{\rho}_b$ evaluated throughout the period of developed, stretched, stable propagation. Equation (5) is then applied to the value of S, except that now the relevant density becomes $\bar{\rho}_b$. Flame speed values of, u_{la}, determined in this way, designated u_{ls}, are closer to those of the PIV values of u_l at zero stretch rate than those based on ρ_b.

The values of α_{cl}, below which the flame becomes unstable, are shown for n-butanol /air at different φ, at 0.1 MPa and 383 K in Fig. 9. The associated PIV based limiting stable values of u_{nr} at this stretch rate are also shown. At lower values of α_{cl}, flames become unstable and faster burning. The filled square symbols and dotted curve shows the stretch-free values, u_{ls}, derived from this modified flame speed method, allowing for $\bar{\rho}_b$ and Le. These are higher than those of u_{nr}. The lower values of Markstein numbers on the rich side, see Section 5.2, contribute to higher u_{nr} values there.

4.4. Radiative heat loss

The flame speed method of measuring u_{la} employs the adiabatic values of both density, ρ_b, and temperature, T_b, with no inherent allowance for either strain rate changes in $\bar{\rho}_{b,}$ or those due to radiative energy loss. The PIV method has no such restrictive assumptions and the associated changes in the burning velocity are embodied in the measurements of S_n and u_g. Radiative heat loss in laminar flames has been computed by several researchers. Zheng Chen et al. [26], found u_{la} for CH_4/air mixtures, to be reduced by the radiation, and decreased by up to 5% and 4% for φ = 0.6 and 1.4, respectively. For completeness, mathematical modeling of laminar flames requires the effects of flame stretching and radiative energy loss or gain to be included, along with the detailed chemical kinetics and flow patterns. Such modelling shows radiative heat loss to decrease the burning velocity. The decrease in temperature slows the propagation rate, and the burned gas cooling generates an inwards flow [27]. Santner et al. [28] have shown that in an atmospheric heptane/air flame, reductions in burning velocities due to radiative energy loss are less than 1% between φ = 0.9 and 1.5. Reductions increase as the lean and rich flammability limits are approached.

Based on their chemical kinetic modelling, Hao Yu et al. [29] have presented generalised empirical expressions for the reductions in burning velocities of hydrocarbon /air mixtures, as a result of this energy loss under a variety of conditions. The measured burning velocities were subjected to radiative loss. In [29] these losses were calculated for seven different fuels, at different temperatures and pressures. The authors mentioned that this empirical correlation could be used with other fuel/air mixtures, except diluted mixtures. This approach was adopted in the present work and losses were calculated as in [29], and added to the PIV values of u_l at α = 0 for the different mixtures. To demonstrate what the hypothetical value of burning velocity would be like in the absence of radiative loss, the calculated loss in burning velocity was added to u_l to give u_{lr}.

5. Discussion

5.1. Values of laminar burning velocity

The increases in values of u_l to u_{lr}, in the absence of radiative loss, are shown by the filled triangles on the ensuing Figs. 10-13. These are expressed as % increases in the first column of Table1. This Table covers three different aspects of the full range of mixtures, at atmospheric pressure. The second column shows the K_{cl} values, marking the onset of instability, whilst the third shows the increases in u_{la} to u_{ls} that occur with the revised flame speed method of processing.

Table 1. Extent of Radiative Loss, Critical Karlovitz numbers, and Strain Rate/Le Flame Speed corrections at atmospheric pressure.

	Radiative loss % Increase in PIV u_l with no radiative loss				Critical Karlovitz number ($K_{cl} \times 10^3$)				Flame Speed Method % Increase in u_{la} to u_{ls} due to strain/Le			
φ	CH_4	i-C_8H_{18}	C_2H_5OH	n-C_4H_9OH	CH_4	i-C_8H_{18}	C_2H_5OH	n-C_4H_9OH	CH_4	i-C_8H_{18}	C_2H_5OH	n-C_4H_9OH
0.7	3.1			1.8	37.8			22.4	-0.9			3.1
0.8	2.0	1.5	1.1	1.5	32.1	9.4	7.9	21.2	-0.9	1.8	1.1	5.0
0.9	1.6	1.4	1.0	1.2	18.5	11.6	6.8	20.0	-0.9	1.6	1.1	4.2
1.0	1.4	1.3	0.9	1.1	15.4	12.4	8.2	17.4	-0.5	1.4	1.8	6.2
1.1	1.4	1.3	0.9	1.0	22.3	13.1	8.9	21.7	1.1	2.7	1.4	5.0
1.2	1.6	1.4	0.9	1.0	25.2	14.3	9.5	25.6	1.0	2.3	1.3	4.3
1.3	2.1	1.7	1.0	1.1	37.7	18.2	10.3	26.7	1.1	3.2	3.6	7.3

Although a stable, un-stretched, flame is an unrealistic concept, the complementary values of u_l provide a useful datum which, along with, Markstein numbers, provides realistic mass burning velocities within the stable flame regime. Such stretch-free values of laminar burning velocities are shown as a function of φ for different fuels in Figs. 10-13. Full line curves, and cross symbols, show PIV values of u_l, based on u_n. Broken curves, and circle symbols, show flame speed method values, u_{la}, based on S_n values from the PIV measurements, extrapolated to $\alpha = 0$, and employing ρ_b in Eq. (5). Values of u_{ls} at α =0, derived from the alternative flame speed method, based on $\bar{\rho}_b$ and Le, are shown by the filled square symbols. These values are higher than those of u_{la}, values of the original, broken curve, flame speed method. They are almost equal to the u_l values of the PIV method. These increases are given in the final column of Table 1. Some of the highest values of u_l are given by the u_{lr}, filled triangles, with no radiative loss.

Figure 10 for CH_4/air mixtures, over a wide range of equivalence ratios at 300 K and 0.1 MPa, presents PIV values of u_l and ρ_b-based flame speeds values of u_{la}. Points for u_{ls} and u_{lr} also are shown. Values of Le for lean mixtures range from 0.96 to 0.99, and for rich mixtures it is 1.1 [23, 24]. Because values of Le are close to unity, the u_{ls} correction is small. The closeness of the u_l and u_{ls} curves indicates the near equality of $\bar{\rho}_b$ from the former and ρ_b from the latter. The increases in PIV values due to the elimination of radiative loss, indicated by u_{lr}, also are rather small. There is close agreement between the two methods, although the u_l values, are always higher. This is because the strain rate correction is small, and there is negligible correction for an increase in the value of $\bar{\rho}_b$ due to the small radiative cooling. Allowance for this could bring the values of u_l and u_{la} closer together. Values of u_{la} from other workers also are shown. The values from [32] are noticeably higher. This might be due to the pressure being recorded, in the absence of flame photographs, and a lack of coordination in flame front imaging and pressure measurement [35].

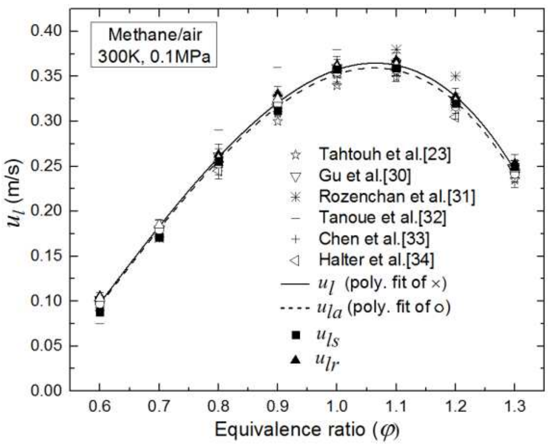

Fig. 10. Unstretched laminar burning velocities, u_l, u_{la}, u_{ls} and u_{lr} for methane/air mixtures at 0.1 MPa and 300 K. Shown also data from literature.

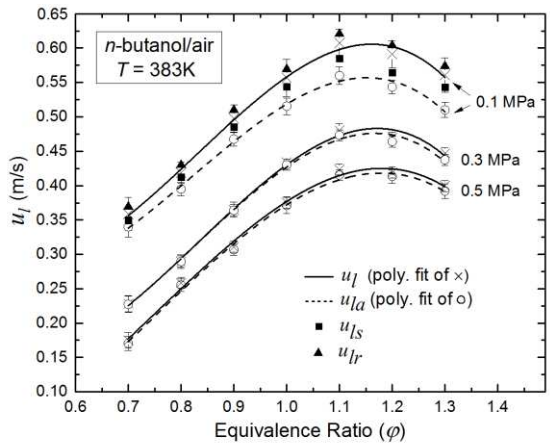

Fig. 11. Unstretched laminar burning velocities, u_l, u_{la} u_{ls} and u_{lr} for n-butanol/air mixtures at 383 K and different pressures.

Figure 11 shows unstretched burning velocities for n-C_4H_9OH, the fuel chosen to study the effects of pressure changes. Values of Le ranged from 1.35 to 2.1 [25], at 0.1 MPa. The high values of Le create the largest strain rate corrections. Here, the flame speed values, u_{la}, at 0.1 MPa are 4-11% lower than the PIV values, u_l, with greater differences for the rich mixtures. Values of all the burning velocities fall with increasing pressure, but always the u_l values are higher. At 0.1 MPa when the, u_{la}, values are corrected for strain rate and Le, the, u_{ls}, values are closer to the u_l values as shown by the filled square points. Allowance for the radiative loss, at 0.1 MPa, results in the u_{lr} values being the highest. Of particular interest is the narrowing of the difference between the PIV values of u_l and flame speed values of u_{la} with increasing pressure. This can be attributed to values of

$\bar{\rho}_b$ approaching those of ρ_b with increasing pressure, as a result of both the more rapid attainment of equilibrium, and the decreasing values of Le with increasing pressure, see Fig. 8.

Figure 12 shows the unstretched burning velocities u_l and u_{la} for i-octane/air mixtures at 0.1 MPa and 358 K. The u_{la} values are underestimates, with a maximum difference of 6.5% below the u_l values. There is rather more consistency in the atmospheric data for ethanol/air values in Fig. 13. Again, the present results follow a decreasing trend from u_{lr} down to the u_{la} flame speed method based on ρ_b. Table 1 shows ethanol to have the lowest radiative energy loss, and its influence is clearly shown by the filled triangles. The original flame speed method underestimates u_{la}, with a maximum difference of 4.5% with PIV values of u_l.

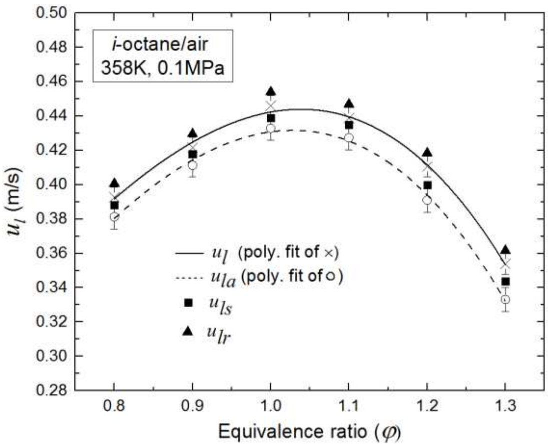

Fig. 12. Unstretched laminar burning velocities, u_l, u_{la}, u_{ls} and u_{lr} for i-octane/air mixtures at 0.1 MPa and 358 K.

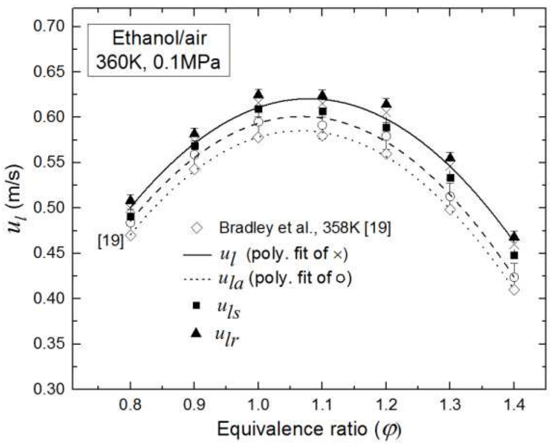

Fig. 13. Unstretched laminar burning velocities, u_l, u_{la}, u_{ls} and u_{lr} for ethanol/air mixtures at 0.1 MPa and 360 K. Shown also data from literature.

5.2 Values of Markstein numbers

With regard to Markstein numbers, all Markstein lengths, based on both S_n and u_{nr}, were found and normalised by the flame thickness, δ. The link between Le and Ma is provided by the early expression of Clavin [9]:

$$Ma = \frac{1}{\gamma} ln \frac{1}{1-\gamma} + \frac{\beta(Le-1)}{2}\left(\frac{1-\gamma}{\gamma}\right) x \int_0^{\gamma/1-\gamma} dx \frac{ln(1+x)}{x}. \quad (11)$$

With K_s and K_c expressing Karlovitz strain, $\delta\alpha_{sr}/u_l$ and curvature, $\delta\alpha_{cr}/u_l$, numbers, a practical form of Eq. (8) is:

$$\frac{u_l - u_{nr}}{u_l} = K_s\, Ma_{sr} + K_c Ma_{cr}. \quad (12)$$

The method of deriving the Markstein lengths from the PIV data is given in Section 4.2. Contrasting Markstein numbers are shown for different φ in Fig.14 for methane/air at 0.1 MPa and in Fig. 15 for n-butanol/air at 0.1, 0.3 and 0.5 MPa. For CH_4/air the influence of small values of Le close to unity has been discussed in Section 5.1. With lean mixtures, values of Le are less than unity, leading to the low Markstein numbers in Fig.14. In contrast, for n-C_4H_9OH/air, with richer mixtures, and O_2 as the minority species, the resulting higher diffusion coefficients creates smaller Lewis numbers, leading to the lower Markstein numbers of Fig.15. With regard to the influence of pressure, Le decreases with increasing pressure, and this leads to the associated decreasing values of both Ma_{sr} and Ma_{cr} in Fig. 15.

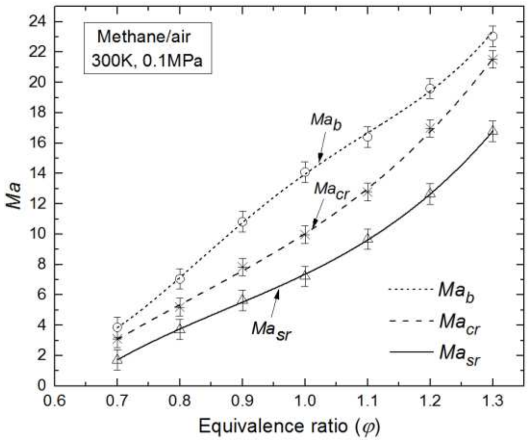

Fig. 14. Variations of Ma_b, Ma_{sr} and Ma_{cr} with φ for methane/air mixtures at 300 K and 0.1 MPa.

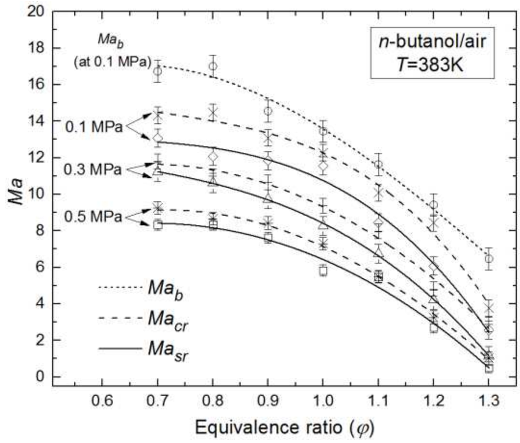

Fig. 15. Variations of Ma_{cr} and Ma_{sr} with φ for n-butanol/air mixtures at different pressures and 383 K.

Values of Markstein numbers for all the other mixtures studied are tabulated in the supplementary material [S3]. There is a significantly greater spread in the reported values of Markstein numbers than in those of burning velocities. This is probably inevitable, due to the problem of evaluating a flame thickness, which is defined by asymptotic end values. Also there are at least three algebraic expressions for flame thickness [36]. In addition, see Section 4.1, there is a probability of up 4-12% underestimation, depending upon the mixture, in the values of L_b. In the present study this is a consequence of the low temperature, 570 K, for the stretch rate isotherm. This degree of underestimation would extend to the different Markstein numbers. Figure 16 shows the measured values of L_b for CH_4/air at 300 K and 0.1 MPa that are referenced in the present paper. These were predominantly determined from the uncorrected flame speed method.

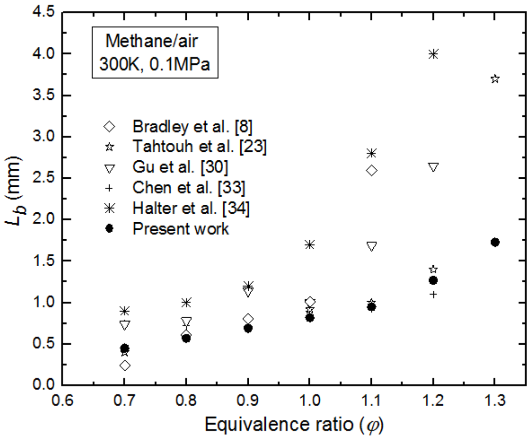

Fig. 16. Flame speed Markstein length, L_b, for methane/air mixtures at 300 K and 0.1 MPa.

6. Conclusions

(i). Stretch-free u_{la} and u_l values have been derived from both flame speed and PIV measurements, respectively. These are valuable, along with Markstein numbers, in expressing practical mass burning velocities, in the stable, stretched flame, regime at stretch rates greater than the critical stretch rate, α_{cl} . They are no guide to the burn rate of developing, unstable, cellular flames at the lower stretch rates.

(ii).Values of $u_{la}, u_l, u_{ls}, u_{lr}, u_{nr}$, Markstein numbers, α_{cl}, and K_{cl} have been found over a full range of φ for methane, n-butanol, i-octane and ethanol mixtures with air. Effects of pressure have been studied for n-butanol/air mixtures.

(iii) The flame speed method of measuring unstretched laminar burning velocity, u_{la}, requires the burned gas density to be known and this is usually assumed to be that of burned gas at equilibrium. In practice, the density is increased by the strain rate and Lewis number during stable propagation, and allowance has to be made for this. This brings such flame speed-derived values of u_{ls} into closer proximity to the PIV-derived values, u_l. This stable stretched flame approach is recommended, in preference to the assumption of adiabatic equilibrium for the burned gas density.

(iv). PIV measurements provide reasonably accurate values of mass burning rate velocities, along with strain rate and curvature Markstein numbers. Greater errors and general variability arise in the measurement of Markstein lengths, due to stretch rate measurements at different isotherms, with higher temperatures preferred. It is estimated that, on this account, the present values of L_b should possibly be increased by between 4 and 12%. Expressions for laminar flame thickness should always be given.

(v). Burning velocity measurements under atmospheric conditions have the aspect of natural phenomena, but corresponding values obtained by mathematical modelling must include the effects of radiative energy loss. Decreases in burning velocities due to radiative energy loss to surroundings at atmospheric temperature are indicated by the differences between the u_{lr} and PIV values of u_l. More generally, radiative energy exchanges might involve energy gain from surroundings at elevated temperatures. Effects of both radiative energy gains and losses in large scale spherical flame propagation are presented in [37].

Acknowledgements

M.E.M thanks the British Council, the Egyptian Cultural and Educational Bureau and the University of Helwan for the financial support of his research. Richard Mumby is thanked for his measurements of schlieren flame speeds.

References

[1] Andrews GE, Bradley D. Determination of burning velocities - a critical review. Combust. Flame 18 (1972) 133-153. https://doi.org/10.1016/S0010-2180(72)80234-7.

[2] Lindow R. An improved burner method for determining laminar flame velocity of fuel gas/air mixtures. Brenst- Warme-Kraft 20(1) (1968) 8.

[3] Bradley D, Hundy GF. Burning velocities of methane-air mixtures using hot wire anemometers in closed vessel explosions. Symp. (Int.) Combust. 13 (1971) 575-583. https://doi.org/10.1016/S0082-0784(71)80059-0.

[4] Jayachandran J, Zhao R, Egolfopoulos FN. Determination of laminar flame speeds using stagnation and spherically expanding flames: molecular transport and radiation effects. Combust. Flame (2014) 2305–2316. https://doi.org/10.1016/j.combustflame.2014.03.009.

[5] Yufei Dong, Vagelopoulos CM, Spedding GR, Egolfopoulos FN. Measurement of laminar flame speeds through digital particle image velocimetry: mixtures of methane and ethane with hydrogen, oxygen, nitrogen, and helium. Proc. Combust. Inst. 29(2) (2002) 1419-1426. https://doi.org/10.1016/S1540-7489(02)80174-2.

[6] Balusamy S, Cessou A, Lecordier B. Direct measurement of local instantaneous laminar burning velocity by a new PIV algorithm. Exp. Fluids 50(4) (2011) 1109-1121. https://doi.org//10.1007/s00348-010-1027-5.

[7] Varea E, Modica V, Vandel A, Renou B. Measurement of laminar burning velocity and Markstein length relative to fresh gases using a new postprocessing procedure: Application to laminar spherical flames for methane, ethanol and isooctane/air mixtures. Combust. Flame 159 (2) (2012) 577-590. https://doi.org/10.1016/j.combustflame.2011.09.002.

[8] Bradley D, Gaskell PH, Xiaojun Gu. Burning velocities, Markstein lengths, and flame quenching for spherical methane-air flames: a computational study. Combust. Flame 104 (1996) 176-198. https://doi.org/10.1016/0010-2180(95)00115-8.

[9] Clavin P. Dynamics behavior of premixed flame fronts in laminar and turbulent flows. Prog. Energy Combust. Sci. 11 (1985) 1-59. https://doi.org/10.1016/0360-1285(85)90012-7.

[10] Bradley D, Mitcheson A. Mathematical solutions for explosions in spherical vessels. Combust. Flame 26 (1976) 201-217. https://doi.org/10.1016/0010-2180(76)90072-9.

[11] Bonhomme A, Selle L, Poinsot T. Curvature and confinement effects for flame speed measurements in laminar spherical and cylindrical flames. Combust. Flame 160 (2013) 1208-1214. https://doi.org/10.1016/j.combustflame.2013.02.003.

[12] Morley C, Gaseq: a chemical equilibrium program, Ver. 0.79 (2005).

[13] Giannakopoulos GK, Gatzoulis A, Frouzakis CE, Matalon M, Tomboulides AG. Consistent definitions of "Flame Displacement Speed" and "Markstein Length" for premixed flame propagation. Combust. Flame 162 (4) (2015) 1249-1264. https://doi.org/10.1016/j.combustflame.2014.10.015.

[14] Bradley D, Hicks RA, Lawes M, Sheppard CGW, Woolley R. The measurement of laminar burning velocities and Markstein numbers for iso-octane–air and iso-octane–n-heptane–air mixtures at elevated temperatures and pressures in an explosion bomb. Combust. Flame 115 (1998)126-144. https://doi.org/10.1016/S0010-2180(97)00349-0.

[15] Dunn-Rankin D, Weinberg F. Location of the schlieren image in premixed flames: axially symmetrical refractive index fields. Combust. Flame 113(3) (1998) 303-311. https://doi.org/10.1016/S0010-2180(97)00233-2.

[16] Beeckmann, J, Hesse R, Schaback J, Pitsch H, Varea E, Chaumeix N. Flame propagation speed and Markstein length of spherically expanding flames: Assessment of extrapolation and measurement techniques. Proc. Combust. Inst. (2018). https://doi.org/10.1016/j.proci.2018.08.047.

[17] Bechtold JK, Matalon M. Hydrodynamic and diffusion effects on the stability of spherically expanding flames. Combust. Flame 67 (1987) 77-90. https://doi.org/10.1016/0010-2180(87)90015-0.

[18] Bradley D. Instabilities and flame speeds in large-scale premixed gaseous explosions. Philos. Trans. Royal Soc. A 357 (1999) 3567-3581. https://doi.org/10.1098/rsta.1999.0510.

[19] Bradley D, Lawes M, Mansour MS. Explosion bomb measurements of ethanol–air laminar gaseous flame characteristics at pressures up to 1.4 MPa. Combust. Flame 156 (2009) 1462–1470. https://doi.org/10.1016/j.combustflame.2009.02.007.

[20] Bradley D, Lawes M, Mumby R, Pervez Ahmed. The stability of laminar explosion flames. Proc. Combust. Inst. (2018). https://doi.org/10.1016/j.proci.2018.07.067.

[21] Clavin P, Williams FA. Effects of molecular diffusion and of thermal expansion on the structure and dynamics of premixed flames in turbulent flows of large scale and low intensity. J. Fluid Mech. 116 (1982) 251–282. https://doi.org/10.1017/S0022112082000457.

[22] Law CK, Cho P, Mizomoto M, Yoshida H. Flame curvature and preferential diffusion in the burning intensity of bunsen flames. Symp. (Int.) Combust. 21 (1986) 1803-1809. https://doi.org/10.1016/S0082-0784(88)80414-4.

[23] Tahtouh T, Halter F, Mounaïm-Rousselle C. Measurement of laminar burning speeds and Markstein lengths using a novel methodology. Combust. Flame 156 (2009) 1735–1743. https://doi.org/10.1016/j.combustflame.2009.03.013.

[24] Lowry W, De Vries J, Krejci M, Petersen E, Serinyel Z, Metcalfe W, Curran H, Bourque G. Laminar flame speed measurements and modeling of pure alkanes and alkane blends at elevated pressures. J. Eng. Gas Turb. Power 133 (9) (2011). https://doi:10.1115/GT2010-23050.

[25] Qianqian Li, Yu Cheng, Wu Jin, Zhaoyang Chen, Huang Z. Study on the laminar characteristics of ethanol, n-butanol and n-pentanol flames. SAE Tech. P. (2015). https://doi.org/10.4271/2015-01-1933.

[26] Zheng Chen. On the accuracy of laminar flame speeds measured from outwardly propagating spherical flames: methane/air at normal temperature and pressure. Combust. Flame 162 (6) (2015) 2442-2453. https://doi.org/10.1016/j.combustflame.2015.02.012.

[27] Zheng Chen. Effects of radiation and compression on propagating spherical flames of methane/air mixtures near the lean flammability limit. Combust. Flame, 157 (2010) 2267-2276. https://doi.org/10.1016/j.combustflame.2010.07.010.

[28] Jeffrey Santner, Has FM, Ju Yiguang Dryer FL. Uncertainties in interpretation of high pressure spherical flame propagation rates due to thermal radiation. Combust. Flame, 161 (2014) 147-153. https://doi.org/10.1016/j.combustflame.2013.08.008.

[29] Hao Yu, Wang Han, Jeffrey Santner, Xiaolong Gou, Chae Hoon Sohn, Yiguang Ju, Zheng Chen. Radiation-induced uncertainty in laminar flame speed measured from propagating spherical flames. Combust. Flame 161(11) (2014) 2815-2824. https://doi.org/10.1016/j.combustflame.2014.05.012.

[30] Xiaojun Gu, Haq MZ, Lawes M, Woolley R. Laminar burning velocity and Markstein lengths of methane–air mixtures. Combust. Flame 121 (1-2) (2000) 41– 58. https://doi.org/10.1016/S0010-2180(99)00142-X.

[31] Rozenchan G, Zhu DL, Law CK, Tse SD. Outward propagation, burning velocities, and chemical effects of methane flames up to 60 atm. Proc. Combust. Inst. 29 (2) (2002) 1461–1470. https://doi.org/10.1016/S1540-7489(02)80179-1.

[32] Kimitoshi Tanoue, Fumio Shimada, Toshiro Hamatake. The effects of flame stretch on outwardly propagating flames. JSME Int. J., Ser. B: Fluids Therm. Eng. 46 (3) (2003) 416–424 https://doi.org/10.1299/jsmeb.46.416.

[33] Zheng Chen, Xiao Qin, Yiguang Ju, Zhenwei Zhao, Marcos Chaos, Dryer FL. High temperature ignition and combustion enhancement by dimethyl ether addition to methane–air mixtures. Proc. Combust. Inst. 31 (1) (2007) 1215–1222. https://doi.org/10.1016/j.proci.2006.07.177.

[34] Halter F, Tahtouh T, Mounaïm-Rousselle C. Nonlinear effects of stretch on the flame front propagation. Combust. Flame 157 (2010) 1825–1832. https://doi.org/10.1016/j.combustflame.2010.05.013.

[35] Hinton N, Stone R, Cracknell R. Laminar burning velocity measurements in constant volume vessels–reconciliation of flame front imaging and pressure rise methods. Fuel 211(2018)446-457. https://doi.org/10.1016/j.fuel.2017.09.031.

[36] Palacios A, Bradley D. Generalised correlations of blow-off and flame quenching for sub-sonic and choked jet flames. Combust. Flame 185, (2017) 309–318. https://doi.org/10.1016/j.combustflame.2017.07.019.

[37] Zheng Chen. Effects of radiation on large scale spherical flame propagation. Combust. Flame 183 (2017) 66-74. https://doi.org/10.1016/j.combustflame.2017.04.031.